

# High Performance Lithium Metal Anode with a Nanolayer of LiZn Alloy for All-Solid-State Batteries

Nicolas Delaporte,<sup>\*[a]</sup> Alexis Perea,<sup>[a]</sup> Steve Collin-Martin,<sup>[a]</sup> Mireille Léonard,<sup>[a]</sup> Julie Matton,<sup>[a]</sup> Vincent Gariepy,<sup>[a]</sup> Hendrix Demers,<sup>[a]</sup> Daniel Clément,<sup>[a]</sup> Etienne Rivard,<sup>[a]</sup> and Ashok Vlijh<sup>[a]</sup>

All-solid-state batteries (ASSB) require stable and safe lithium (Li) metal anode, which needs surface preparation to increase lithium diffusion and impede the formation of dendrites. In this work, the formation of a thin LiZn layer on lithium metal using sputter deposition is reported. This method was selected due to the absence of solvents and by-products generated during the modification, for its rapidity and because the formation of the alloy is performed in a clean and controlled atmosphere. Zinc has been chosen for its low cost and high Li<sup>+</sup> ion diffusion coefficient of the corresponding LiZn alloy that is 1000 times higher than Li. Different parameters for the Zn deposition were

investigated such as the distance between the Zn target and Li foil, the effect of substrate tilt and the direct current applied to the target. Electrochemical performance of LiFePO<sub>4</sub>/solid polymer electrolyte/Li ASSB demonstrated the superiority of the LiZn anodes and the clear influence of deposition parameters on the durability and performance at high C-rates. Scanning electron microscopy images of the cross-sectional view of LFP/SPE/Li stackings extracted from pouch cells after cycling showed an evident migration of Zn into the bulk Li metal anode as well as the formation of AlZn nanoparticles.

## Introduction

Nowadays, lithium-ion batteries (LIBs) largely dominate the rechargeable battery market in the electric vehicles sector due to their high energy density and long-life span.<sup>[1]</sup> However, all solid-state batteries (ASSB) are safer due to the lack of flammable organic components and also offer the potential for a dramatic improvement of energy density.<sup>[2]</sup> In fact, the use of a solid electrolyte, which acts as electrical insulator, ionic conductor and physical barrier for lithium (Li) dendrites, enables the use of Li metal as the anode material.<sup>[3]</sup> Li metal is characterized by a very high theoretical specific capacity (3860 mAh g<sup>-1</sup>) as well as a low redox potential ( $-3.04$  V vs. SHE).<sup>[4]</sup> Therefore, Li metal is paving the way for high energy density batteries that could accelerate the deployment of long-range electric vehicles.<sup>[5]</sup> Thus, an increase in volumetric energy density of up to 70% can be expected in comparison to LIBs still using conventional anode materials.<sup>[6]</sup> Unfortunately, Li metal suffers from large volume changes during cycling with the formation of dendrites and “dead Li” that could lead to internal short-circuit.<sup>[7]</sup> In addition, some interfacial problems remain unresolved in ASSB,<sup>[8]</sup> such as the poor adhesion at the Li-electrolyte interface,<sup>[9,10]</sup> and the high reactivity of lithium with some ceramic electrolytes (e.g., LAGP).<sup>[11]</sup> Moreover, even if in ASSB, the solid electrolyte represents a strong barrier to

slow down the progression of dendrites, in most cases, the Young's modulus of polymer electrolyte is under the threshold value of 6 GPa to suppress the growing of Li dendrites.<sup>[12]</sup>

Many studies in the literature focus on the surface modification of Li metal anode to overcome these different problems. Several approaches are reported for instance to increase the compatibility between the Li metal and the electrolyte, but also their contact; to deposit a layer to avoid the dendrite progression and the formation of high surface area lithium (HSAL); to generate a 3D lithiophilic scaffold to efficiently redistribute the Li ion flux;<sup>[13]</sup> to passivate the surface of the Li metal forming a highly conductive Li salt for stable electrodeposition; or even to form an in-situ lithium-metal alloy in order to reduce the Li nucleation overpotential leading to a dense non-dendrite Li deposition, excellent Coulombic efficiency and ultra-long cycling stability of the batteries. Our group recently published a review paper that lists the different strategies to modify the surface of the Li metal foil.<sup>[14]</sup> Most of them are not easily scalable especially that consisting of the solid electrolyte interface (SEI) formation in a first cell before reassembling a new battery with the passivated lithium foil. For instance, the protection of lithium with a simple polymer layer,<sup>[15]</sup> or with an interlayer of polymer and ceramics such as Cu<sub>3</sub>N/styrene butadiene rubber copolymer (SBR),<sup>[16]</sup> Al<sub>2</sub>O<sub>3</sub>/poly(vinylidene fluoride-co-hexafluoropropylene) (PVDF-HFP)<sup>[17]</sup> or 10-nm Al<sub>2</sub>O<sub>3</sub>/polyimide<sup>[18]</sup> has been shown to be an efficient and simple way to avoid the formation of dendrite. Modification of Li in solution are the most common method due to the highly reductive ability of Li that can react with a lot of molecules to generate plenty of salts, alloys and organic and inorganic compounds such as Li<sub>3</sub>PO<sub>4</sub>,<sup>[19]</sup> Li<sub>3</sub>PS<sub>4</sub>,<sup>[20]</sup> LiF,<sup>[21]</sup> LiCl/Li<sub>3</sub>P,<sup>[22]</sup> Li-Al-O solid-state electrolyte,<sup>[23]</sup> LiF/Li<sub>5</sub>Sn<sub>2</sub>,<sup>[24]</sup> LiCl/LiZn.<sup>[25]</sup> Atomic layer deposition (ALD) is a powerful technique

[a] Dr. N. Delaporte, Dr. A. Perea, S. Collin-Martin, M. Léonard, J. Matton, V. Gariepy, Dr. H. Demers, D. Clément, Dr. E. Rivard, Dr. A. Vlijh  
Center of Excellence in Transportation Electrification and Energy Storage  
1806 Bd. Lionel-Boulet, Varennes, QC, Canada  
E-mail: Delaporte.Nicolas@hydro.qc.ca

 Supporting information for this article is available on the WWW under  
<https://doi.org/10.1002/batt.202200245>

to modify any surface at the nanoscale with a perfect control of the deposited layer thickness, however this method is very long due to several purges/chemicals loadings and reaction cycles needed during the formation of the layer. Some research groups studied the modification of lithium foil via ALD with various compounds among  $\text{Al}_2\text{O}_3$ ,<sup>[26,27]</sup>  $\text{LiF}$ <sup>[28]</sup> or  $\text{ZrO}_2$ .<sup>[29]</sup> To efficiently suppress the dendrite progression, carbon layers are also deposited on the surface of the lithium foil, for instance by lamination with a self-standing multiwalled carbon nanotubes film,<sup>[30]</sup> by reaction with a graphene oxide solution to generate a graphene film after spontaneous reduction<sup>[31]</sup> or simply by magnetron sputtering technique leading to an amorphous carbon coating.<sup>[32]</sup> Although the aforementioned techniques of modification are promising to expand the life of the Li anode, the cost during scaling, the problem of repeatability/reproducibility, long reaction times, the need for extremely dry and harmful solvents are limiting factors for their wide use in industry.

Another promising route to modify the surface of the lithium foil is via sputtering method. This method is simple and rapid to perform nanometric deposition of conductive and non-conductive materials such as metals (e.g., Zn, Au) and oxide ceramics ( $\text{Al}_2\text{O}_3$ ,  $\text{Li}_3\text{PO}_4$ ) for instance. Depending on the deposition parameters, relatively compact and uniform layers can be obtained. The reproducibility is also easily obtained, in contrast to some modifications in liquid medias or by applying a coating of polymer with a filler (carbon or ceramics for instance). In addition, the deposition is performed with high purity sputtering targets (99.9% to 99.9999%) under controlled atmosphere with high vacuum after several purges with inert gas (commonly argon), thus limiting the contamination during deposition. Furthermore, this is a dry method, in consequence no additional costs for solvents, their storage/elimination and no drying step of the sample is needed after deposition. Finally, industrial roll-to-roll sputtering machines for large scale applications exist today and could be easily tuned for surface modification of lithium foil.<sup>[33,34]</sup> This technique is already widely used in the energy storage field, for instance for the preparation of silicon anodes,<sup>[35,36]</sup> to study solid-state electrolytes (e.g.  $\text{Li}_{0.5}\text{La}_{0.5}\text{Ti}_{1-x}\text{Al}_x\text{O}_3$ ,<sup>[37]</sup>  $\text{Li}_7\text{La}_3\text{Zr}_2\text{O}_{12}$ ,<sup>[38]</sup>), to protect the positive current collector from corrosion (e.g.  $\text{Cr}_x\text{N}$ <sup>[39]</sup> or  $\text{TiN}$ <sup>[40]</sup> layers), for solid oxide fuel cell<sup>[41]</sup> or lithium-sulfur<sup>[42]</sup> applications, to coat the surface of electrode materials (e.g., nanocrystalline Si coated with amorphous Si<sup>[43]</sup>), and especially for the preparation of all solid-state thin-film lithium-ion batteries.<sup>[44–48]</sup>

Recently, the sputtering method was applied to the surface modification of lithium anode. Wang et al. reported that the deposition of an ultrathin  $\text{Li}_3\text{PO}_4$  layer gives a homogeneous current density distribution for uniform lithium deposition instead of dendrites thanks to  $\text{Li}_3\text{PO}_4$  isotropy amorphous nature.<sup>[49]</sup> A 20-nm thick  $\text{Al}_2\text{O}_3$  protected lithium anode showed a much better cycling performance than the bare one due to the “surfactant” role played by the ceramic layer facilitating a homogeneous Li nucleation and the growth of a smooth layer-by-layer film.<sup>[50]</sup> Instead of ceramics, metals (M) can be deposited to form  $\text{Li}_x\text{-M}_y$  alloys on the surface of the electrodes.

This concept is interesting since most of Li alloys possess higher Li diffusion coefficient than pure lithium, which contributes to enhanced electrochemical kinetics and reduces the dendrites growth.<sup>[51]</sup> In addition, Li-rich alloys limit the parasitic reactions between the anode and the electrolyte<sup>[52]</sup> and could be more air-stable than pure lithium facilitating their manipulation and storage in dry room.<sup>[53]</sup> Several metals to date have been sputtered on Li metal such as Al,<sup>[53]</sup> Si,<sup>[54]</sup> Cu,<sup>[55]</sup> Au<sup>[56]</sup> and Zn.<sup>[56,57]</sup>

In this work, we report the modification of lithium foils with a nanometric layer of Zn deposited by sputtering. Zn has been chosen for its relatively low price and because the LiZn alloy has a high  $\text{Li}^+$  ion diffusion coefficient of  $4.7 \times 10^{-8} \text{ cm}^2 \text{s}^{-1}$ , which is superior to that for pure lithium (i.e.,  $5.69 \times 10^{-11} \text{ cm}^2 \text{s}^{-1}$ ).<sup>[57]</sup> The formation of a LiZn alloy upon deposition of Zn metal was confirmed by X-ray diffraction (XRD) analysis. Different parameters for the Zn deposition were investigated such as the distance between the Zn target and the lithium foil, the effects of substrate tilt angle and direct current (DC) applied to the target. Atomic force microscopy (AFM) and scanning electron microscopy (SEM) images revealed that the particles size slightly varied with the sputter conditions selected, however the morphology of Li grains was deeply impacted. The electrochemical performance of the bare and modified lithium anodes was assessed with all-solid-state  $\text{LiFePO}_4$  (LFP)/solid polymer electrolyte (SPE)/Li pouch cells. The cycling was performed at 50 °C up to 1C. The cells made with the Zn-coated Li anodes showed improved performance at high C-rates while the reference cells were not able to cycle under a constant current of 1C. The specific capacity remained perfectly stable for 26 cycles at 1C for the best sample (denoted 20-45-25°). This cycling represents a strong improvement in comparison to the reference cell, which begins to fail during cycling at C/2. SEM images of the cross-sectional view of LFP/SPE/Li stackings extracted from pouch cells after cycling showed an evident migration of Zn into the bulk Li metal anode as well as the formation of AlZn nanoparticles. Finally, we report for the first time an interesting observation concerning the influence of deposition parameters on the variation of texture of certain Li grains, which will be more detailed in a future study.

## Experimental Section

### Preparation of lithium metal foils coated with Zn thin film

The 50-μm thick lithium foil (containing 0.2% of Al) is provided by Hydro-Quebec. The Zn film was deposited on the lithium surface by using an EM ACE600 table-top coater from Leica equipped with a double sputter head and a glow-discharge option for sample cleaning. The Zn target of 99.9% purity with a diameter of 54 mm and a thickness of 1.0 mm was purchased from Micro to nano company. The lithium foil was placed in the deposition chamber and six sequences of vacuum up to 0.008 Pa and refilling with highly pure Ar (grade 6.0, 99.999% purity) were realized before deposition. Then, the metallic target was cleaned applying a pre-sputter current of 70 mA for 30 s to remove contaminants on its surface. The DC magnetron sputtering was performed in the

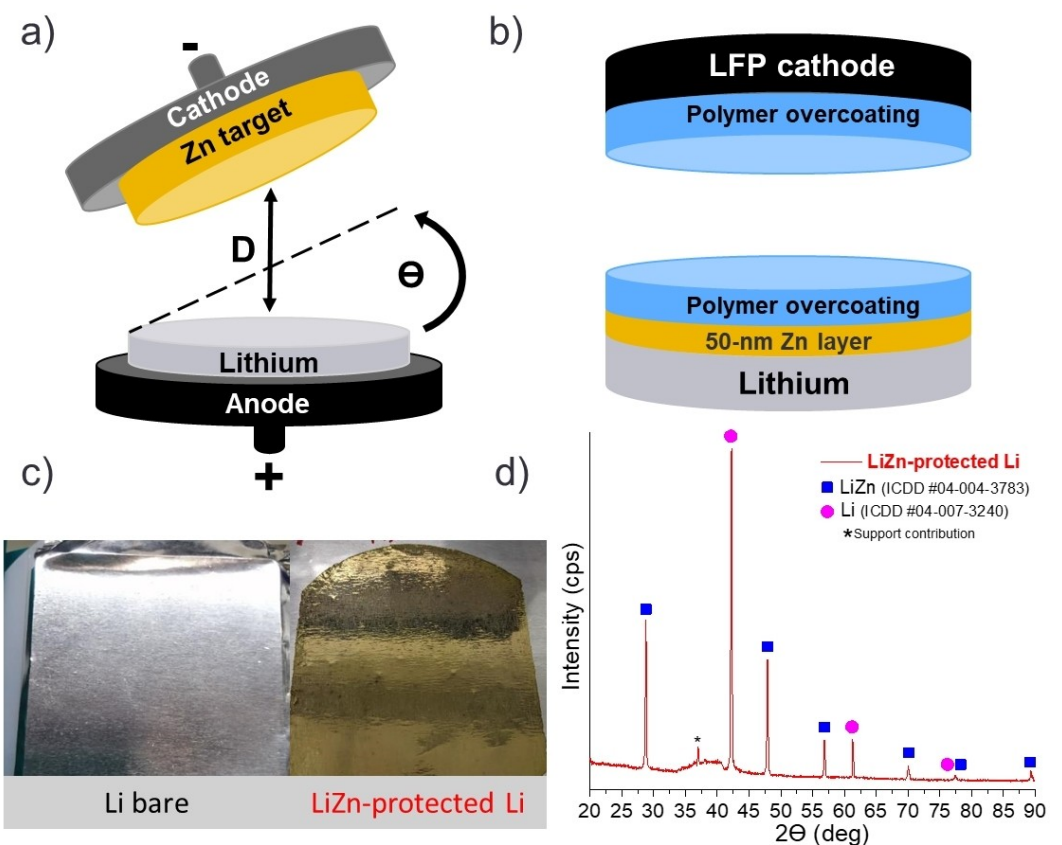


**Figure 1.** a) Schematic representation of the sputter chamber. The sputter current is applied on the cathode, the distance  $D$  between the substrate to be modified and the Zn target can be adjusted as well as the inclination of the stage [tilt angle ( $\Theta$ )]. b) Schematic representation of the cell configuration used: the unmodified or the Zn-modified Li anode is coated with a thin polymer layer (~15  $\mu\text{m}$ ) and laminated on an LFP cathode overcoated with 20  $\mu\text{m}$  of polymer. c) Photographs of Li bare (left) and LiZn-protected Li (right) foils. d) XRD pattern for the LiZn-protected Li foil.

vacuum chamber under a pressure of 0.8 Pa in an inert atmosphere of Ar. In the process of sputtering, the stage was continuously rotated to reach the best uniformity of deposition, the rotation was set to 20 rotations per min. Different parameters for the deposition were tested. Various DC currents were applied to the Zn target varying from 15 to 50 mA. The distance  $D$  between the substrate and the Zn target was also adjusted between 45 to 70 mm (See Figure 1a for the schematic representation of the sputter chamber). The inclination of the substrate (tilt angle  $\Theta$ ) is varied from 0° to 25° (parallel to the target).

The rate of deposition was monitored with a quartz crystal microbalance (QCM) and comprised between 0.26 to 1.7  $\text{nm s}^{-1}$  depending on the deposition parameters chosen. Table 1 resumes the different Zn-coated Li anodes fabricated with the various deposition parameters employed (sputter current, tilt angle  $\Theta$  and target-sample distance  $D$ ), which were evaluated in battery (other samples were prepared but not tested in battery due to non-uniformity of deposit). Each lithium sample is named as follow: X-Y-Z°, where X represents the DC current applied, Y the distance between the Zn target and the lithium foil and Z is the tilt angle. For instance, the modified lithium denoted 20-45-25° is fabricated using a sputter current of 20 mA at 45 mm from the Zn target with an inclination of 25°.

### Preparation of LFP electrodes

Carbon-coated LFP powder (75.3 wt.%), carbon black (1 wt.%), LiTFSI salt (6.27 wt.%) and a PEO polymer (19.23 wt.%) were mixed

**Table 1.** List of the different Zn-coated Li anodes electrochemically tested in pouch cells (C-rate protocol). The various deposition parameters employed [sputter current, target-sample distance ( $D$ ) and tilt angle ( $\Theta$ )] are listed as well as the samples names.

Sample name	Sputter current [mA]	Distance $D$ [mm]	Tilt angle $\Theta$ [°]
15-45-0°	15	45	0
15-45-8°	15	45	8
15-45-17°	15	45	17
15-45-25°	15	45	25
20-45-0°	20	45	0
20-45-8°	20	45	8
20-45-17°	20	45	17
20-45-25°	20	45	25
50-45-0°	50	45	0
50-45-8°	50	45	8
50-45-17°	50	45	17
50-45-25°	50	45	25
50-60-0°	50	60	0
50-70-0°	50	70	0
30-45-0°	30	45	0
30-60-0°	30	60	0

using proper amount of an acetonitrile/toluene (80:20 v/v) solvent mixture. The slurry was cast on a carbon-coated aluminum foil (15  $\mu\text{m}$ ) to have an active mass loading of 8  $\text{mg cm}^{-2}$  after drying. The process was conducted inside a dry room with a dew point less than  $-50^\circ\text{C}$ . The electrodes were conserved in a metal plastic bag in dry atmosphere before being utilized.

### Polymer casting on lithium and LFP electrodes

Polyethylene oxide (m.w. ~100,000) was dispersed in a small amount of anhydrous tetrahydrofuran (THF from Sigma-Aldrich) that was mixed until a viscous solution was obtained. Lithium bis(trifluoromethanesulfonyl)imide salt (LiTFSI from Sigma-Aldrich) corresponding to a O:Li molar ratio of 25:1 was then added to the polymer solution with 40 wt.% of tetraethylene glycol dimethyl ether (TEGDME, from Sigma-Aldrich) based on the polymer mass. Finally, 0.4 wt.% of Omnirad 651 photoinitiator (from IGM resins) was dispersed in the polymer solution. The whole is intensely mixed until a homogenous and bubble-free solution was obtained.

The solid polymer electrolyte (SPE) was casted on the cathode and anode surfaces using doctor blade technique. The wet thickness is adjusted depending on the dry thickness desired after drying (~20 µm on the cathode and 15 µm on the lithium). LFP and lithium foils were dried in a ventilated hood for 5 min and in an oven at 50°C for 5 min to remove the excess of THF. Then, the electrodes were placed in a sealed box purged with dry nitrogen for 3 min and exposed to UV light (300 WPI) at 50 cm for 5 min. The cross-linked electrodes were conserved in a metal plastic bag in dry atmosphere before being utilized.

### Pouch cells assembling and electrochemical testing

Figure 1b presents the cell configuration employed during the pouch cells assembling. The overcoated anodes are hot-pressed with the overcoated LFP cathode at 80°C under vacuum for 3 min. The active surface area in contact between the two electrodes is ~7.48 cm<sup>2</sup>. All the LFP/SPE/Li stackings were prepared in a dry room (dew point < -50°C) and then placed in a special casing for applying an isostatic pressure of 75 psi and a constant temperature of 50°C.

The batteries were electrochemically evaluated with a BioLogic BCS-815 potentiostat. Two formation cycles at C/12 were performed prior to the rate capability tests. The galvanostatic charge/discharge cycles were recorded with different current densities corresponding to C-rates of C/12, C/6, C/4, C/3, C/2 followed with a cycling stability at 1C. The electrochemical tests were performed at 50°C in the potential window ranging from 2.0 to 3.8 V vs. Li/Li<sup>+</sup>. Following cycling stability, two batteries were stopped after five cycles at 1C and disassembled to be observed with a scanning electron microscope (SEM).

Electrochemical impedance spectroscopy measurements of the cells were performed with an AC amplitude of 10 mV and a frequency range of 0.01 MHz to 50 mHz. Nyquist plots were recorded at open circuit potential (OCP) after the two formation cycles at C/12.

### Characterizations

XRD analysis for the bare and Zn-coated lithium foils was performed in a dry room (dew point < -50°C) using a SmartLab X-ray diffractometer (Rigaku) with Co K $\alpha$ 1 radiation ( $\lambda = 1.78892 \text{ \AA}$ ). Data were collected between 20° and 90° with a scan speed of 2.29° min<sup>-1</sup>. The surface of lithium foils is ~15 mm<sup>2</sup> (thickness ~50 µm, square shape) and the spot analyzed is ~5 mm<sup>2</sup>.

Optical images and depth profiles of various deposits on lithium and silicon surfaces are obtained with a Keyence VK-x200 3D laser microscope at 5× or 150× magnifications.

AFM images of various Zn deposits on silicon wafer were obtained with a Bruker Dimension Icon AFM operating in ScanAsyst air mode using silicon nitride tips. The resolution was 512 samples/

line. The spring constant of the cantilever was 0.4 N m<sup>-1</sup> and the scan rate 0.50–0.97 Hz. The morphology of the same deposits is also observed with a magnification of 200k $\times$  using a Hitachi SU-7000 scanning electron microscope.

Cross-section views of LFP/SPE/Li stackings extracted from pouch cells after cycling at 1C were observed using a Hitachi SU-7000 scanning electron microscope with an EDS windowless detector Oxford Instruments Ultim Extreme 100 mm<sup>2</sup> which can detect Li X-ray.<sup>[58]</sup> Samples were prepared in a dry chamber and inserted in the SEM located inside the dry room to minimize external contamination. The micrograph and X-ray map were acquired at an accelerating voltage of 5 kV, a probe current of 500 pA and a working distance of 9 mm.

## Results and Discussion

### Validation of Zn coating thickness and formation of LiZn alloy

Figure 1(c) shows the photographs for the pristine Li foil (left) and a LiZn-protected Li foil (right). The bare lithium presents a metallic grey color while after Zn deposition via sputtering, a homogeneous gold color was observed, which is typical of a LiZn alloy.<sup>[57]</sup> Depending on the deposition conditions, a slight change in the intensity of gold color is observed that suggests a difference of texture for the LiZn layers. In reality, even if visually the surface seems homogeneous, various intensities of gold are present depending on the crystalline grain. This point will be discussed below.

To confirm the presence of an alloy, XRD analysis was performed on the LiZn-protected Li foil. Figure 1(d) presents the XRD pattern. The peaks for the lithium metal (card number of the International Centre for Diffraction Data, ICDD: #04-007-3240) and the LiZn alloy (ICDD: #04-004-3783) are both present confirming the in-situ formation of the alloy upon deposition of Zn. Small peaks between 35°–40° are attributable to the XRD support used for the analysis as put in evidence with the corresponding XRD pattern in Figure S1(a) (see Supporting Information), and that of pristine Li foil (Figure S1b). It is worth noting that no metallic oxides (e.g., ZnO) and no other Li<sub>x</sub>Zn<sub>y</sub> alloys are detected that excludes the hypothesis that the variation of gold color could be attributed to another alloy, which was preferably formed on a crystalline surface rather than another.

The mass deposited during Zn sputtering is monitored using a quartz crystal microbalance (QCM) that is situated at the center of the stage. The rate of deposition was comprised between 0.26 to 1.7 nm s<sup>-1</sup> depending on the deposition parameters chosen. Then, when the deposition rate is known, the lithium foil was placed on the entire stage surface for being modified for a predefined time in order to reach the desired thickness. The thickness of Zn coatings is systematically verified to be sure this parameter is well controlled. To do this, the sputtering was firstly performed on a perfectly flat Si wafer. Figure 2(a) shows a photograph of the Si wafer with supposed 50-nm thick Zn lines.

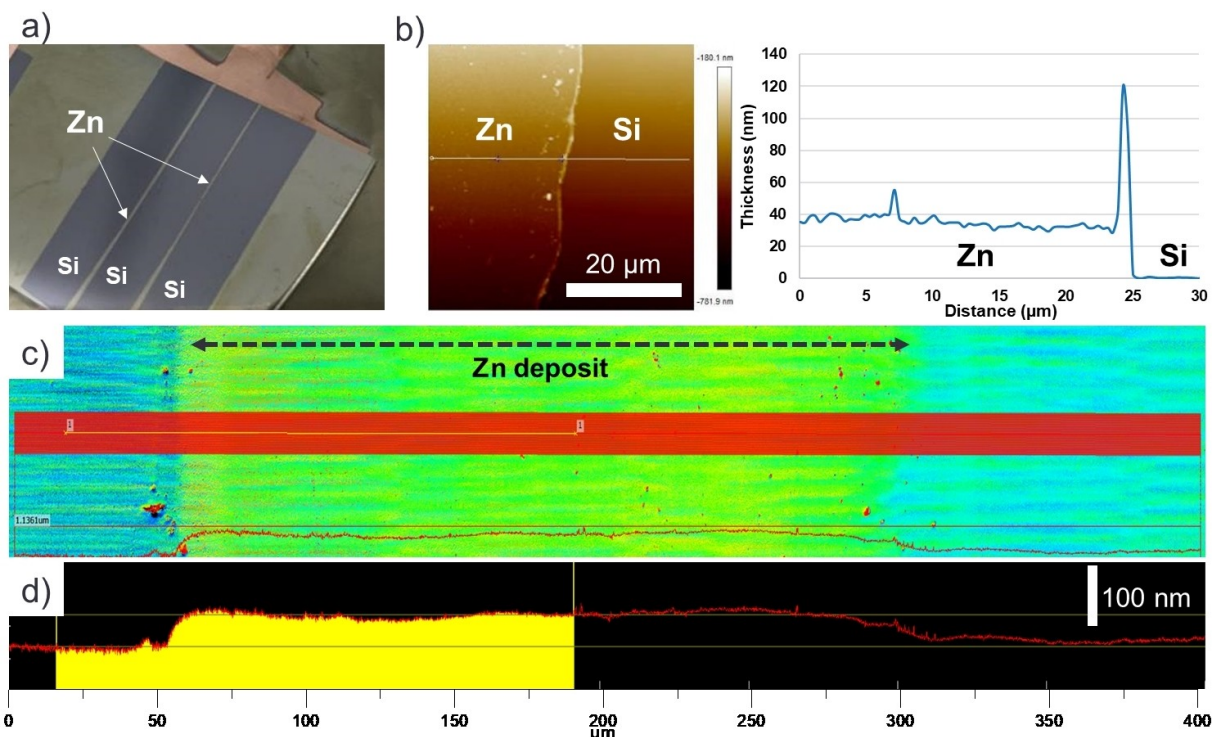


**Figure 2.** a) Photograph of the Si wafer with thin Zn lines used to determine the metal thickness. b) AFM image and depth profile of the Zn deposit. c) Laser scanning confocal image and d) corresponding depth profile (average on 60 measures) of a supposed 50-nm thick Zn deposit on a Si wafer.

The thickness of the Zn coating was firstly estimated by means of the AFM. Figure 2(b) shows an AFM image of the Zn deposit on the Si wafer with the corresponding depth profile. A region straddling the coated and uncoated areas of the sample was selected and swept. A sharp height peak at the border between the two regions is observed. Although this peak is most likely a measurement artefact, the tracking on either side was excellent which brings confidence as to the accuracy of the results. To highlight the difference in height between the coated and uncoated regions, the data were numerically manipulated. A plane was fitted to the Si region by regression and the perpendicular distance between this plane and the height datapoints was calculated. A maximum of 40 nm is obtained for the Zn deposit. However, due to the proximity with the mask used to protect the Si surface, the thickness of Zn is surely underestimated as it can be seen with the depth profile obtained from the laser scanning confocal image (Figure 2c and d). In fact, the Zn thickness slowly increases at the coating extremities to reach a plateau near of the theoretical thickness of 50 nm determined with the QCM. Figure 2(c) presents the laser scanning confocal image of the same Zn coating on Si wafer. The deposit is approximately 250- $\mu$ m large and represented in green. To determinate the Zn thickness, 60 measurements are performed, and an average depth profile is obtained as represented in the Figure 2(d). This method gives approximately 49 nm for a supposed 50-nm thick Zn deposit, in good accordance with the value anticipated by QCM. Hence, the confocal method is preferred to rapidly estimate or validate the thickness of Zn deposits.

## Electrochemical performance of LiZn-protected lithium anodes

### Optimal LiZn coating thickness

A first study was conducted to determine the optimal Zn thickness on lithium surface to achieve the best electrochemical performance and reproducibility. Coin-cells were assembled with a LFP cathode (the same described in the Experimental section), a self-standing PEO-based solid polymer electrolyte without plasticizer and the bare or modified lithium anodes. The preparation of the SPE as well as the coin-cells assembly is well explained in a recent study.<sup>[59]</sup> LiZn-protected Li metal electrodes with various Zn thicknesses from 8 to 114 nm were prepared. The galvanostatic cycling at C/3 at 50°C for these batteries is presented in the Figure S2. It was found that a 50-nm thick Zn deposit was enough to give the best performance and this parameter was kept constant to study the influence of tilt angle ( $\Theta$ ), target-substrate distance ( $D$ ) and sputter current.

### Cell format and cycling protocol used for Li anodes validation

It was decided to compare the potential of modified Li anodes to cycle at high C-rates rather than study their long-term stability at constant charge/discharge current density. In fact, most of ASSB manufacturers, such as QuantumScape, are focused on reaching commercial targets for their single-layer

solid-state pouch cell, which include for example high battery capacity (typically in the range of  $2.5\text{--}5\text{ mAh cm}^{-2}$ ) as well as cycling at high C-rates (charge/discharge = 1C/1C) at low temperature ( $25\text{--}30^\circ\text{C}$ ).<sup>[60]</sup>

The cyclability at C/3 for 100 cycles for LiZn-protected Li anodes was still studied in coin-cells at  $50^\circ\text{C}$  using a self-standing PEO-based solid polymer electrolyte. The long-term stability for the Li bare (reference) and a LiZn-protected Li anode (denoted 50-45-0°, see Table 1 for details) is represented in Figure S3. Superior stability was obtained for the cell assembled with the modified electrode showing a 92% retention of initial capacity after 100 cycles with a stable Coulombic efficiency while the reference cell showed a higher capacity loss per cycle during cycling and died after less than 60 cycles.

Special electrode preparation and cells assembling described in the Experimental section and Figure 1(b) are used to study the various LiZn-protected Li anodes produced. Polymer overcoatings on LFP cathode and Li anode permit to create an optimized interface between the electrodes and the solid polymer electrolyte reducing the overall cell resistance. Pouch cell assembling with a monitoring of the pressure (75 psi) is preferred to the coin-cell format in term of performance and reproducibility.<sup>[61]</sup> In addition, the surface of lithium metal used is larger in pouch cells (i.e.,  $\sim 14\text{ cm}^2$  in this study) than in the conventional CR2032 coin-cell type (i.e.,  $\sim 2\text{ cm}^2$ ) and the electrochemical results are then more representative and realistic. This electrode fabrication and cell format used permit to cycle LFP/SPE/Li cells up to 1C in charge at  $50^\circ\text{C}$  (at least when modified Li anodes are used) that is remarkable performance for ASSB.

For each LiZn-protected Li anode studied in this work, at least two pouch cells were assembled to check the reproducibility. The Figure S4 in the Supporting Information presents the discharge capacity at various C-rates and corresponding Coulombic efficiency for different LFP/SPE/Li batteries assembled with the Li bare (reference) and a LiZn-protected Li anode (denoted 30-45-0°, see Table 1 for details). The reproducibility is very well whether a modified Li foil or the pristine lithium was utilized. For better clarity, only one cycling per cell will be presented in the manuscript.

### Influence of tilt angle

A lot of different parameters can change the compositions, properties and textures of films deposited by DC sputtering. For instance, the substrate used can impact the nature and crystallinity of the deposit,<sup>[62]</sup> the composition/concentration of inert gases employed can affect the particles size,<sup>[63]</sup> the film porosity can be tuned by varying the substrate tilt angle,<sup>[64]</sup> the chemistry and morphology of the film can be changed by using reactive gases (e.g.,  $\text{O}_2$ ,<sup>[65]</sup>  $\text{N}_2$ <sup>[62]</sup>), or again the sputtering rate, sputtering pressure and substrate temperature can strongly impact the surface roughness and grain sizes of the coating.<sup>[66]</sup>

The first parameter investigated in this study is the substrate tilt angle ( $\Theta$ ) (see Figure 1a). Figure 3 shows the electrochemical performance for different LFP/SPE/Li batteries assembled with the Li bare (reference) and four LiZn-protected Li anodes. The modified Li electrodes were made by sputtering Zn metal varying the substrate tilt angle from 0° to 25° (parallel to the Zn target). Figure 3(a) presents the discharge capacity obtained at various C-rates for the cells assembled with the different anodes. At low C-rates, all the batteries delivered  $\sim 160\text{ mAh g}^{-1}$ , which is the practical discharge capacity for this carbon-coated LFP.<sup>[67]</sup> The capacity remains quite stable up to a C/2 cycling rate for the cells made with the modified Li anodes, while a capacity loss starts to be visible for the reference cell. At 1C, a sudden drop of the discharge capacity is observed mainly due to the poor electrical conductivity of the LFP cathode. The batteries were still able to deliver  $\sim 95\text{--}105\text{ mAh g}^{-1}$  during the discharge process for the first cycles at 1C. However, the discharge capacity was not stable at all upon cycling for the reference cell that oscillated between 70 and  $95\text{ mAh g}^{-1}$ . Note that this behavior is reproducible, the cycling for a second reference cell is shown in Figure S4(a and b). In contrast, during 20 cycles at 1C rate, the cells assembled with the modified Li anodes presented a relatively stable discharge capacity even if the batteries with LiZn-protected Li anodes made by Zn sputtering with a low tilt angle (electrodes 20-45-0° and 20-45-8°) show an obvious decrease of capacity after 12–15 cycles at 1C. It seems that more the tilt angle increases and more the cycling stability at high C-rate is better. This behavior is confirmed looking at the corresponding Coulombic efficiency plotted in Figure 3(b). Up to a cycling rate of C/2, the

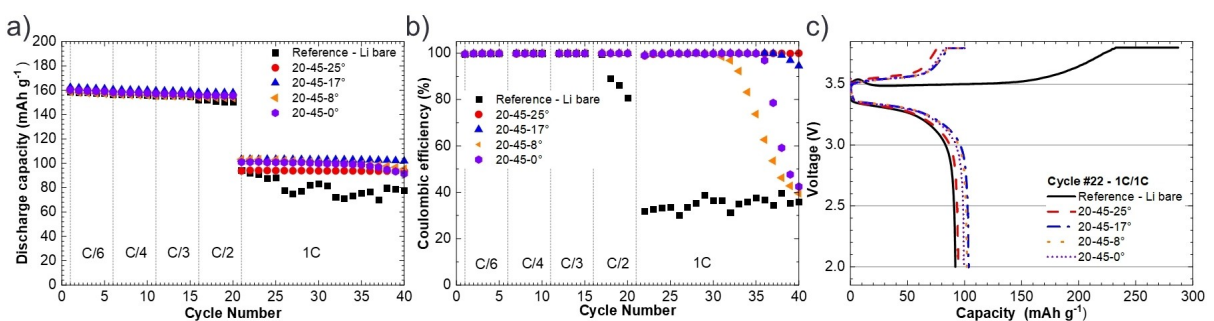


**Figure 3.** a) Discharge capacity at various C-rates, b) corresponding Coulombic efficiency and c) charge/discharge profile for the first cycle at 1C (22<sup>nd</sup> cycle) for different LFP/SPE/Li batteries assembled with the Li bare (reference) and four LiZn-protected Li anodes. The influence of the tilt angle ( $\Theta$ ) is compared [constant sputter current = 20 mA, and constant target-substrate distance ( $D$ ) = 45 mm].

Coulombic efficiency is near of 100% for all cells made with the modified Li electrodes. In contrary, a drop of its value is observed at each cycle at C/2 for the reference cell and significative of the generation of lithium dendrites. At 1C, the Coulombic efficiency completely fall to reach 20%–40% for the reference cell. For the batteries assembled with the modified anodes, the cycling at 1C remained stable (in term of Coulombic efficiency) for 9, 14, 16 and more than 20 cycles for the lithium anodes made with tilt angles of 8°, 0°, 17° and 25°, respectively. A clear tendency shows that effectively more the tilt angle is high and more the stability at high C-rate is long. At high C-rates, with a PEO-based electrolyte, the generation of Li dendrites is inevitable without surface modification of Li anode. Figure 3(c) presents the charge/discharge profile for the first cycle at 1C (22<sup>nd</sup> cycle) for the different batteries. The galvanostatic profiles for the cells assembled with the modified Li electrodes clearly indicate the single and long reversible plateau around 3.4 V vs. Li/Li<sup>+</sup>. This corresponds to the electrochemical activity of Fe<sup>3+</sup>/Fe<sup>2+</sup> in the ordered olivine structure based on the two-phase reaction between LiFePO<sub>4</sub> and FePO<sub>4</sub>.<sup>[68]</sup> The charge profile for the reference cell is unusual and the specific capacity of ~230 mAh g<sup>-1</sup> obtained is well above the theoretical capacity of the LFP cathode material (~165 mAh g<sup>-1</sup>). This long plateau is always present during the charge when the Li<sup>+</sup> ions cross the SPE from the cathode to the lithium anode surface, which inevitably leads to the formation of Li dendrites at high cycling rate. This phenomenon is often observed by an arbitrary appearance of "voltage noise" and characteristic of micro-short-circuits.<sup>[69]</sup> The charge capacity is higher than the theoretical one because the conventional delithiation of the cathode is counter-acted by dendritic lithiation caused by a dendrite.<sup>[70]</sup> In conclusion, the absence of long plateau during charge and the stable Coulombic efficiency for the cells made with the modified Li anodes is a clear indication than the LiZn layer slows down the formation of dendrites, at least for few cycles at 1C.

Figure S5(a) shows the AFM images of 50-nm thick Zn layers on Si wafers deposited with various tilt angles, respecting the same conditions than for the modification of Li surface. The grains form and size do not substantially change when the tilt angle varies between 0° and 25°, although a clear influence of this parameter is observed visually on the gold color obtained at the surface of the Li foil (this point will be discussed below) as well as on the electrochemical performance. The same conclusion is reached when observing the different deposits with a SEM (see Figure S6a), the surface is composed of nanometric cubic or spherical particles (~15–45 nm). Engwall et al. fabricated a special substrate holder permitting the AuTa deposition through various angles ranging from 0° to 90°.<sup>[64]</sup> The authors conclude that film properties depend weakly on substrate tilt until a critical tilt angle that lies in the range of 40°. Then, the morphology change (at least at this scale) is not well appreciated in the tilt angle range chosen in our study and is probably not the main factor involves in the electrochemical performance variations.

Additional electrochemical results for LiZn-protected Li anodes fabricated applying a constant sputter current of 50 mA

are available in Figure S7. The sample made with the tilt angle to 0° presents the worst stability at 1C.

### Influence of sputter current

The second parameter investigated in this study is the sputter current applied to the Zn target. Various sputtering currents were evaluated between 15 to 70 mA. When a current of 70 mA is applied, the lithium surface is not homogenous and consequently this lithium anode was not electrochemically evaluated because in this case, the formation of the LiZn alloy layer is not reproducible. The minimum current applicable to ignite the plasma and etch the surface of Zn target was of 15 mA. A series of lithium foils was prepared keeping a distance of 45 mm, a sputter current of 15 mA and varying the tilt angle (see Table 1 for details, samples denoted 15–45-X°, X = variable). Under these conditions, the coating at the lithium surface did not seem total even by changing the substrate tilt angle. Nevertheless, batteries were assembled with these modified anodes and the corresponding cycling data are presented in Figure S8. Without surprise, the electrochemical performance is similar than for the reference cell and all the batteries were not able to cycle at 1C. However, at C/2 the modified batteries still cycled correctly while the reference cell presented micro-short-circuits. This highlighted the importance of perfect covering of the anode surface to have a positive impact in battery.

The more interesting results were obtained for lithium foils modified with a sputter current comprised between 20 and 50 mA. In this range, uniform surfaces were obtained. The electrochemical performance for batteries assembled with lithium anodes modified with a sputter current of 20, 30 and 50 mA [constant target-substrate distance ( $D$ )=45 mm, and constant tilt angle ( $\Theta$ )=0°] are presented in Figure 4. The result show that lower sputtering currents yield better cyclability. In fact, the batteries cycled at 1C without short-circuit for 11, 12 and 14 cycles, when the LiZn coating was formed with a sputter current of 50, 30 and 20 mA, respectively. This behavior is obviously explained by the better homogeneity of the Li surface when a low sputter current is employed. At the nanoscale, AFM and SEM images do not show significant variation in the grain sizes (see Figures S5b and S6b). A slight increase in size of Zn nanoparticles (up to 55 nm in diameter) is visible for the film made at 70 mA. However, at the microscale the surface roughness is affected by the sputter current. Figure S9 presents the depth profiles from laser scanning confocal images of 50-nm thick Zn layers deposited with the various sputter currents (from 20 to 70 mA). For the sample prepared with a sputter current of 20 mA, the surface is relatively flat with a variation of thickness inferior to 10 nm between the upper and the lower points. When the current was increased to 30 and 50 mA, the roughness of the coating slightly increased. With 70 mA, a strong variation of the surface thickness was observed (see Figure S9d) with sometimes 20 nm of difference between the upper and the lower points within the surface film. These morphological observations are in good

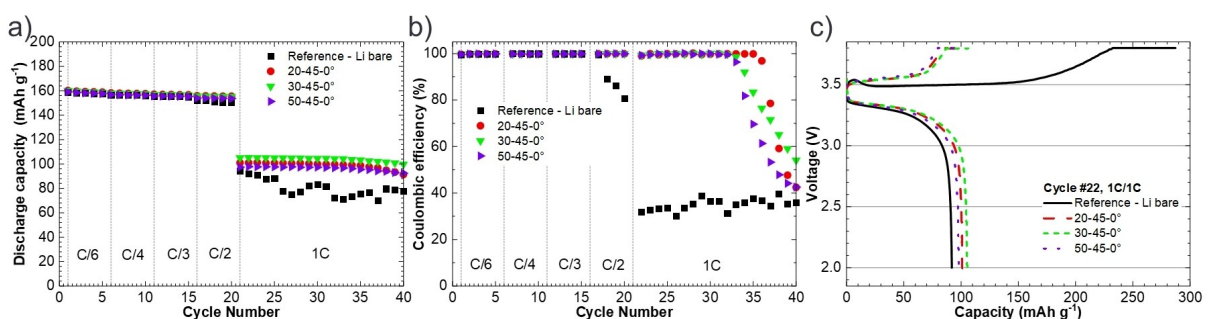


**Figure 4.** a) Discharge capacity at various C-rates, b) corresponding Coulombic efficiency and c) charge/discharge profile for the first cycle at 1C (22<sup>nd</sup> cycle) for different LFP/SPE/Li batteries assembled with the Li bare (reference) and three LiZn-protected Li anodes. The influence of the sputter current is compared [constant target-substrate distance ( $D$ ) = 45 mm, and constant tilt angle ( $\Theta$ ) = 0°].

accordance with the electrochemical results obtained, which assume that lower sputter current yields better homogeneity of the film and cyclability at high C-rate.

It is worth noting that the deposition rate is strongly impacted by the sputter current utilized. In fact, using a current of 20, 30, 50 and 70 mA led to a deposition rate of 0.46, 0.62, 1.1 and 1.7 nm s<sup>-1</sup>, respectively. It is well known that the deposition rate has an influence on the grain size as well as on the roughness of surface film, even if in some cases, the grain size remains quasi similar while the roughness increases with the increase of the deposition rate as reported by Paul et al.<sup>[66]</sup> These observations are similar of what we obtained in the present study.

#### Influence of target-substrate distance

The last parameter investigated in this study is the variation of the target-substrate distance. Figure 5 shows the electrochemical performance for batteries made with LiZn-protected Li anodes produced by varying the distance between 45 and 70 mm and keeping the sputter current (50 mA) and the tilt angle (0°) constant. All the modified batteries were able to cycle correctly at 1C for several cycles but rapidly when the distance increases, the stability decreases. For instance, the batteries assembled with Li anodes made with target-substrate distances of 45, 60 and 70 nm achieved 11, 9 and 6 cycles at

1C, respectively, with a stable Coulombic efficiency. This result is correlated with the quality of the coating, in fact, a short target-substrate distance is better to reach a certain homogeneity of the coating. Especially, when low currents are used, typically under 30 mA, increasing the distance above 45 mm led to a really poor quality of the lithium surface. For this reason, these samples were not tested. The quality of the LiZn layer is optimal when 45 mm is selected due to the increase of sputtered particles flux striking the substrate and the higher intensity of the plasma in contact with the sample surface. The same conclusion is obtained for batteries cycled with modified lithium anodes fabricated with a sputter current of 30 mA and target-substrate distances of 45 and 60 mm. The corresponding cycling is shown in Figure S10. The sample named 30-45-0° (see Table 1 for detail) ran correctly for 13 cycles while that denoted 30-60-0° failed after 6 cycles. The lithium produced at 30 mA with a distance of 70 mm was not tested due to the poor quality of the film and the non-reproducibility of the modification.

#### Best LiZn-protected Li anode

Finally, the best sample in term of electrochemical performance is the modified lithium named 20-45-25° (see Table 1 for sputtering conditions). This result matches well with the previous conclusions made: a low sputter current is preferable

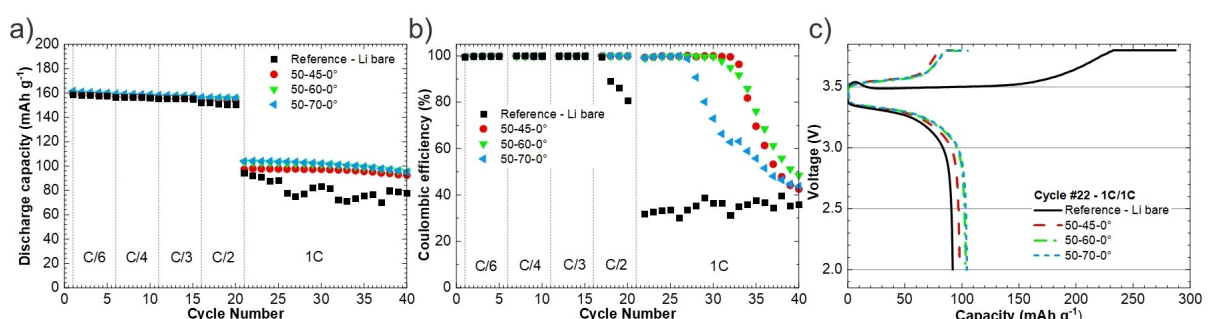


**Figure 5.** a) Discharge capacity at various C-rates, b) corresponding Coulombic efficiency and c) charge/discharge profile for the first cycle at 1C (22<sup>nd</sup> cycle) for different LFP/SPE/Li batteries assembled with the Li bare (reference) and three LiZn-protected Li anodes. The influence of the target-substrate distance ( $D$ ) is compared [constant sputter current = 50 mA, and constant tilt angle ( $\Theta$ ) = 0°].

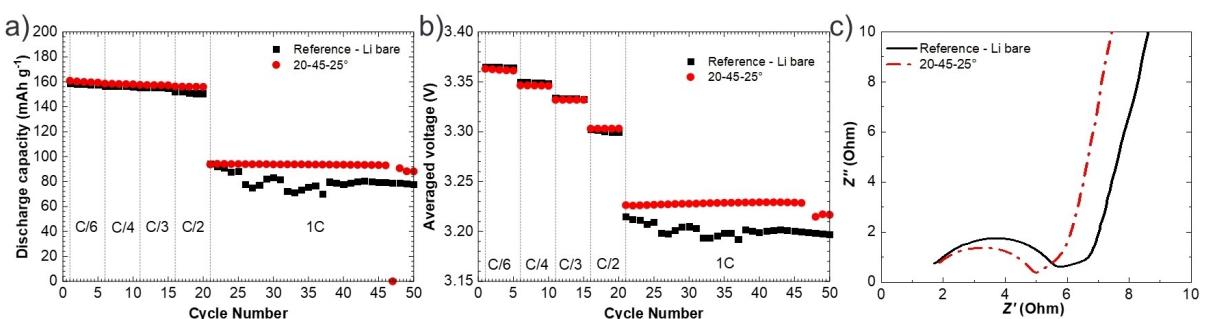
(15 mA is not suitable), a high substrate tilt angle is recommended (the most parallel to the Zn target) and a short target-substrate distance is better to reach a certain homogeneity of the coating. Figure 6(a) shows the discharge capacity at various C-rates and especially at 1C until the battery fails. The discharge capacity remained perfectly stable for 26 cycles at 1C that represents a strong improvement in comparison to the reference cell, which begins to fail during cycling at C/2. Note that this cycling at high C-rate is remarkable for a ASSB with a Li anode and without optimization of the electrolyte and cathode. This demonstrates the importance of Li passivation to reach stable cycling with high current densities, mandatory for a potential industrial application. Figure 6(b) presents the average voltage of the discharge profile recorded during cycling for the reference cell and the modified battery assembled with the LiZn-protected Li anode. At 1C, the value of average voltage for the modified cell remained perfectly stable until a dendrite appeared. The Nyquist plots recorded after the formation cycles for the same batteries are presented in Figure 6(c). The electrolyte resistance value (i.e.,  $\sim 1.5 \Omega$ ) was determined from the intercept of the semicircle on the real axis at high frequency. The same value was obtained for the two batteries since the same SPE was utilized. A semicircle in the high-middle frequency region is observed, and its diameter on the horizontal axis ( $Z'$ ) is approximately equal to the charge-transfer resistance through the electrode/electrolyte interface.<sup>[71]</sup> This resistance is also similar for the two cells and about  $3.5\text{--}4.3 \Omega$ . At lower frequencies, another small semicircle hardly visible is present and associated to the intrinsic lithiation resistance i.e., the feasibility of the  $\text{Li}^+$  ions to react with the active material.<sup>[72]</sup> Finally, the straight-line domain in the low frequency region is associated with the diffusion of lithium ions into the bulk of the electrode. The impedance spectra are very similar for both electrodes confirming that the strongly improved performance for the modified battery is effectively attributable to the efficient role of the LiZn alloy layer to prevent the formation of dendrites at high C-rates.

#### Post-mortem SEM observations of aged LFP/SPE/Li batteries

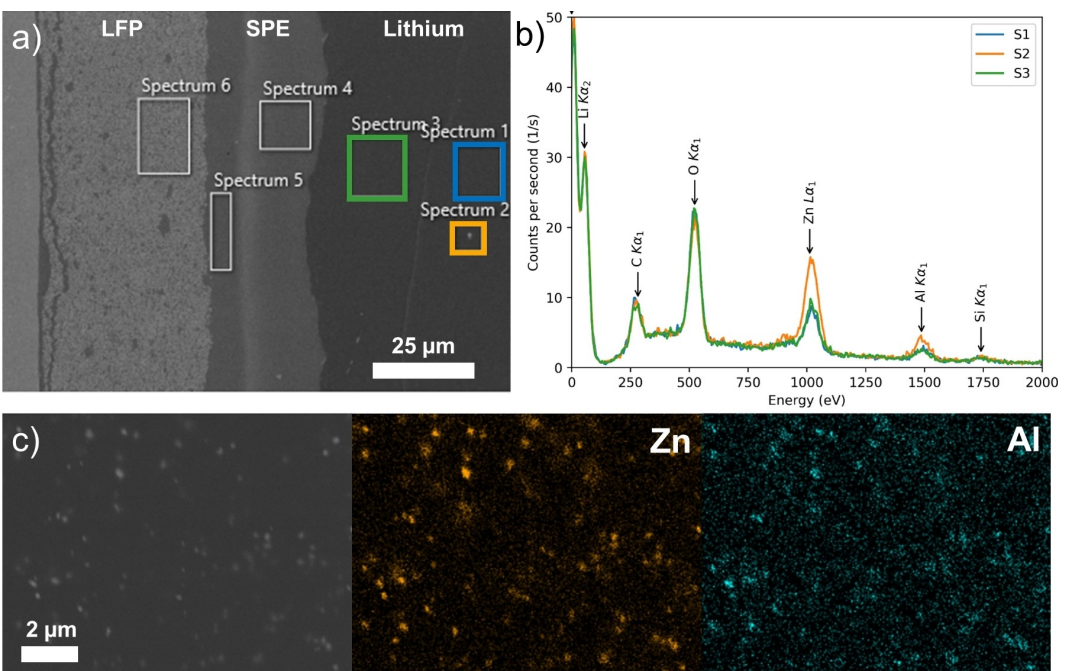
SEM images of the cross-sectional view of LFP/SPE/Li stackings extracted from pouch cells after cycling at 1C are shown in

Figure S11. The cells were assembled with the Li bare anode (Figure S11a) and a LiZn-protected Li electrode (Figure S11b). The cathode was intact after cycling with no migration of LFP particles inside the SPE. Some carbon aggregates are visible even if visually the cathode appeared smooth and uniform. For the SPE, clearly the two polymer layers coated on the electrodes surface are identifiable and were revealed during the sample preparation. However, as put in evidence with EDX mapping of the SPE, available in Figure S12, the composition is similar for the two regions. The most important difference is concerning the SPE on the lithium side. For the cell assembled with the modified anode (Figure S11b), the SPE/lithium interface seems well conserved, even after harsh cycling at 1C, with slight Li inclusions in some places into the SPE. In contrary, for the reference cell, a strong deformation on the lithium side is observed that is consistent with the formation of dendrites, the long plateau in charge and the low Coulombic efficiency observed during cycling at 1C. The damaged areas created by the growing/dissolution of Li dendrites are mainly composed of Li metal and Li salt as evidenced by EDX analysis (spectrum available in Figure S13 in the supporting information).

Figure 7(a) presents the SEM cross-section view of the LFP/SPE/Li stacking assembled with the LiZn-protected Li anode after cycling at 1C. EDX spectra corresponding to three areas in the lithium foil and represented with colored squares in the SEM image are shown in Figure 7(b). Spectra 1 and 3 are very similar in composition. C, O and Si are coming from sample preparation for SEM observation. The lithium electrode is homogeneously composed of Al, which is initially present as doping metal. In addition, it was found that the Zn metal migrates into the bulk Li anode during cycling that is consistent with observations made by Samsung.<sup>[73,74]</sup> In order to increase the durability of the batteries at 1C, future works will focus on the fabrication of more stable and thicker metal layers to keep a kind of buffer alloy layer permitting fast  $\text{Li}^+$  ion transport and uniform Li electrodeposition. The EDX spectrum 2 was acquired on a region with an unidentified particle visible inside the orange square of Figure 7(a). Interestingly, the relative concentration of Zn and Al in this area in comparison to other elements was increased, suggesting the presence of an AlZn-rich particle. A closer view of the Li bulk electrode is shown in Figure 7(c) with the corresponding elemental mapping of Zn and Al. The presence of a multitude of nanometric particles rich



**Figure 6.** a) Discharge capacity at various C-rates and b) average voltage of the discharge profile recorded during cycling for the reference battery assembled with the Li bare and the cell made with the modified Li anode (20-45-25°). c) Nyquist plots recorded after the formation cycles for the two batteries.



**Figure 7.** a) SEM cross-section view of an LFP/SPE/Li stacking assembled with a LiZn-protected Li anode (sample 20-45-25°) after cycling at 1C. b) EDX spectra corresponding to three areas in the lithium foil represented with colored squares in the SEM image (spectrum 1, S1 in blue; spectrum 2, S2 in orange and spectrum 3, S3 in green). c) SEM image and corresponding elemental mapping for Zn and Al of the lithium foil after cycling at 1C.

in Zn and Al was confirmed, although these two elements are still present everywhere inside the Li electrode. Because of the presence of high electric field and local heating at the micro- and nano-protrusions during cycling, Zn atoms become mobile (since Zn has a low melting point) even at nominally room temperature, thus segregating and forming islands. Zn has more affinity for Al than for Li, once AlZn aggregates are formed, Zn segregates or dissolves in the Li bulk electrode. It is why Zn and Al seems dispersed everywhere in the electrode but in the same time form AlZn nanoparticles. To deeply understand this phenomenon and its kinetics, post-mortem SEM analyses should be performed after different stages of cycling. In fact, especially under cycling, this whole system is neither stable thermodynamically nor kinetically. Metals segregation in alloys is well known and widely reported in the literature.<sup>[75]</sup> For instance, Zn segregation at the grain boundaries of an Al-Zn-Mg-Cu alloy during aging has been recently observed by Zhao et al.<sup>[76]</sup> More specifically, a recent study shows that engineering of segregation of Zn atoms in an Al-Zn alloy via severe plastic deformation (SPD process) enhances the diffusion and grain-boundary sliding and leads to the occurrence of room-temperature superplasticity.<sup>[77]</sup>

#### Influence of lithium grains on the surface morphology of Zn coating

A last paragraph is devoted to a particular observation made after Zn deposition that is important to be addressed. To the best of our knowledge this point was never approached in any study dealings with surface modification of lithium metal.

Figure 8 presents optical images with a magnification of a) 150× and b) 10× for a 50-nm thick Zn layer deposited on lithium surface. Even if visually the LiZn alloy layer seems uniform after deposition by sputtering, as shown in Figure 1(c), clearly some Li grains appeared more or less dark. More specifically, some grains present a dark gold color with a surface full of holes while those with a light gold color are smoother or presenting only some holes.

The first hypothesis was that the color changes were related to various  $\text{Li}_{x}\text{Zn}_y$  alloys formed on Li surface influenced by the crystal orientations of Li metal. During the impact of the substrate surface with Zn particles, the formation of a precise alloy with its own morphology would occur depending on the crystal orientation. It is known in the battery domain that the crystal orientations of current collector affect the electrodeposition of various metal as well as the texture and nature of the deposit.<sup>[78]</sup> For instance, Ishikawa et al. showed that the electrodeposition of Li metal is more homogenous on the Cu (111)-oriented grains rather than on polycrystalline Cu.<sup>[79]</sup> This feature is important since a homogenous Li deposit is effective for the suppression of dendrites. Another study demonstrated that the SEI thickness (related to the facility of electrolyte decomposition) on the Cu surface was the thinnest on single-crystal Cu (111). In addition, the composition of the SEI was different following the crystal orientation. The authors suggested that the orientation dependence of electrochemical activity plays an important role in the formation of the SEI layer.<sup>[80]</sup> Similarly, we first thought that a similar phenomenon happens during the metal deposition on the surface of the lithium foil. However, the XRD pattern for the LiZn-protected Li foil (see Figure 1d) only reveals the presence of a LiZn alloy.

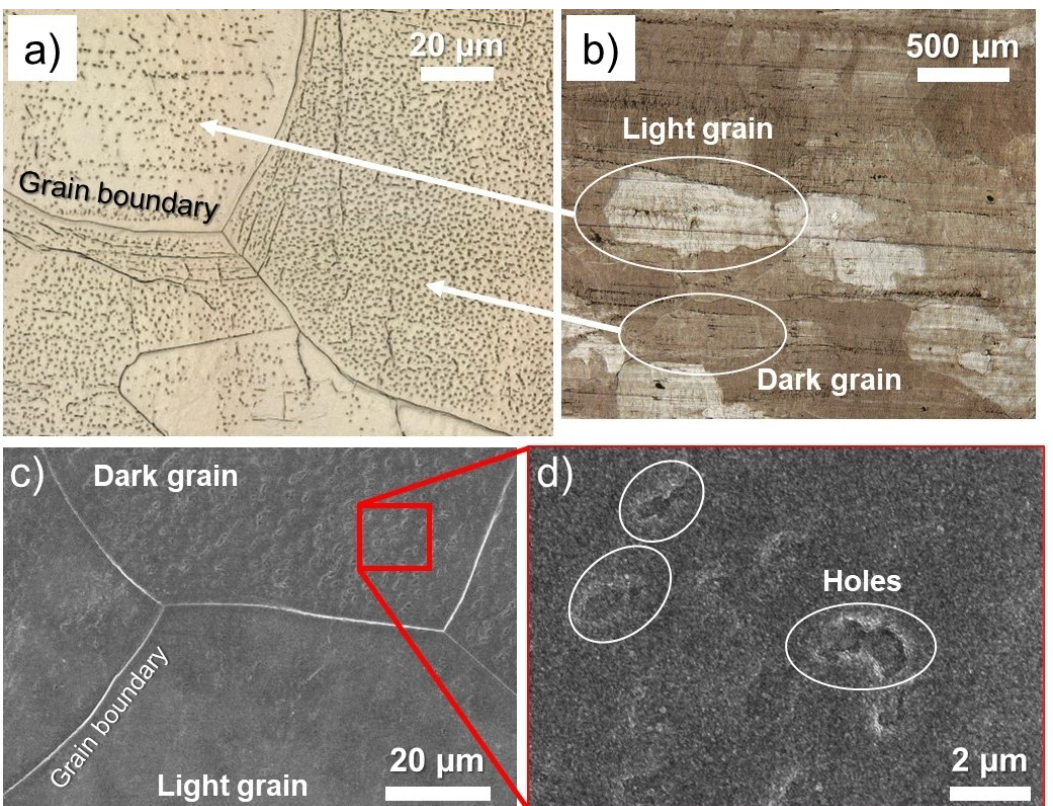


**Figure 8.** Optical images with a magnification of a) 150× and b) 10× for a 50-nm thick Zn layer deposited on lithium surface. Some grains present a dark gold color with a surface full of holes while those with a light gold color are smoother or presenting only some holes. SEM images of the LiZn-protected Li surface with a magnification of c) ×1,200 and d) ×10,000. Holes are well visible at the surface of the dark grain and absent for the light one.

Thus, the difference of color is not related to different chemistries of surface. But clearly, the morphology of the deposit varies from a grain to another, as put in evidence with the optical image of Figure 8a. Inside a dark grain, the holes are uniformly scattered everywhere respecting the grain boundaries. Figure 8 shows SEM images of the LiZn-protected Li surface with a magnification of c) ×1,200 and d) ×10,000. The surface of the modified lithium is composed of the nanometric cubic or spherical particles (see Figure S6) and the diameter of holes is typically in the range of 1–3 µm. We tentatively tried to correlate this phenomenon (holes apparition) with the Li grains crystal orientation. To do this, electron backscatter diffraction (EBSD) mapping of the Li surface was performed before Zn deposition and the crystal orientation map has been compared with an optical image of the same region after sputtering (results not shown). After several attempts, no clear conclusions were reached between crystal orientation and texture. At this stage, this phenomenon seems random and a future study in depth will be devoted specially to the understanding of these observations.

However, some tendencies are clearly visible concerning the apparition of these holes. Figure S14(a) presents optical images (5× magnification) of 50-nm thick Zn layers deposited on lithium surface with various tilt angles and with a sputter current of 20 mA. At low tilt angle, typically 0°, the surface of lithium is rather homogeneous, the gold color is quasi the

same for all the Li grains. But more the substrate tilt angle is increased and more the apparition of holes and various gold color is visible. The same trend was observed for Zn depositions performed with a sputter current of 15 mA (see Figure S15 in the Supporting Information). Optical images of the Li surface with a magnification of 150× (Figure S15b) clearly show the gradual apparition of the holes when the tilt angle is increased. Similarly, more the sputter current is increased for a fixed tilt angle and distance, and more the grain heterogeneities appeared. Figure S14(b) presents the optical images (5× magnification) of LiZn-protected Li anodes produced with a constant distance of 45 mm, a tilt angle of 0° and varying the sputter current from 15 to 70 mA. Finally, a trend is also visible when the substrate-target distance is changed. As shown with optical images of modified Li surfaces fabricated with a distance of 45 and 70 mm [see Figure S16, constant sputter current=30 mA and constant tilt angle ( $\Theta$ )=0°], more the distance is short and more the holes/color differences appear.

After reflection, we assume these holes are produced by a local heat production happening during the sputtering process. During the deposition, the temperature of the substrate gradually increases due to the energetic particle (electrons, atoms, ions, molecules and even clusters) bombardment on the surface of the substrate. In fact, the stage is not cooled and even if the substrate holder equipped with a thermocouple shows a negligible increase of the temperature upon Zn

deposition, in reality at the sample surface the temperature increases rapidly. Toku et al. studied the effect of substrate temperature (no intentional substrate heating) on the crystalline structure of  $\text{TiO}_2$  thin films deposited on silicon.<sup>[81]</sup> It was found that under specific deposition conditions, the sample surface can reach more than 200 °C. The authors demonstrated that it is possible to obtain crystalline films growth in low temperature sputtering process, only by varying the deposition parameters. Most likely, such a surface heating is also obtained during the deposition of Zn at the surface of lithium. Since this metal melt easily (~180 °C), liquid holes are formed and gradually evaporated during Zn sputtering in the chamber under partial vacuum. The fact that some Li grains preferably present these holes could be attributed to the heterogeneous surface of this metal. In fact, within the grains on the surface there are kinks, steps, edges, dislocations, impurity inclusions, vacancies, and other defects. The result of this “surface zoo” of inhomogeneities is that under the energetic particle bombardment, different nano-to micro-metric regions undergo bond breaking at different rates (local metal-metal bond breaking at the atomic level takes place first which leads to surface diffusion and then local melting). In conclusion, the kinetics of melting at these various heterogeneities are different that leads to a mosaic of textures/morphologies upon Zn deposition. This theory seems to be supported by the optical images of LiZn-protected Li foils obtained by varying the deposition conditions (Figures S14–S16). In fact, the holes apparition is more important for short substrate-target distances, when the sample is parallel to the Zn target (i.e., 25°) and for high sputtering currents. Simply, in these conditions, the striking of the Li surface with the sputtered particles flux is maximal and the local melting of Li is more important revealing the different grain colors.

A study is ongoing to understand this phenomenon and will be useful to predict and favor the generation of a precise  $\text{Li}_x\text{M}_y$  alloy (M being a metal) upon deposition at different substrate temperatures.

## Conclusion

In this work, the modification of lithium foils with a nanometric layer of Zn deposited by sputtering is reported. Zn has been chosen for its relatively low price and because the LiZn alloy has a high  $\text{Li}^+$  ion diffusion coefficient.<sup>[57]</sup> The presence of the LiZn alloy was confirmed by XRD analysis. Various sputter deposition parameters were investigated such as the substrate-target distance, the substrate tilt angle and sputter current utilized. AFM and SEM images revealed that the particles size slightly varied with the sputter conditions selected, however the morphology of Li grains was deeply impacted. All-solid-state LFP/SPE/Li batteries made with the Zn-coated Li anodes showed improved performance at high C-rates, especially at 1C, when the reference cell was not able to cycle correctly. The specific capacity remained perfectly stable for 26 cycles at 1C for the best sample (i.e., 20-45-25°), which is remarkable performance for ASSB. This special cell preparation and

assembling permit to rapidly validate the potential for a modified lithium anode to impede the formation of dendrites. The sputter conditions clearly impacted the cyclability at 1C and even if initially we thought the smoothest surface would permit to reach the best electrochemical conditions, in reality, it was not the case. In fact, the best LiZn-protected Li anode presents strong morphological variations at its surface. For the first time, we report an interesting observation concerning the influence of sputter conditions on the variation of morphology of Li grains. Such a comprehension of reactions occurring at the Li surface was not discussed in any scientific paper on this subject.<sup>[53–57]</sup> A more detailed study is ongoing to confirm the hypotheses presented in this paper. Finally, it was found that Zn metal migrates into the bulk Li anode during cycling that is consistent with the observations made by Samsung.<sup>[73,74]</sup> In addition, AlZn nanoparticles were also formed during the cycling coming from a reaction between Zn nanoparticles and Al initially presents in the lithium foil.

In conclusion, the LiZn interlayer clearly has a role of 3D lithiophilic host for fast  $\text{Li}^+$  transfer between the solid electrolyte and the Li bulk has well explained in the work of Ouyang et al.<sup>[82]</sup> They mixed Zn nanoparticles in molten Li to generate LiZn alloy rods providing multiple lithiophilic sites for uniform lithium deposition. However, the durability of the alloy interlayer is compromised by the inevitable and progressive Zn dissolution in the Li bulk upon cycling and especially at high C-rates. For this reason, the protection works well for several cycles until the complete dissolution of the initial LiZn layer. In order to increase the durability of the batteries at 1C, future works will focus on the fabrication of more stable and thicker metal layers to keep a kind of buffer alloy layer permitting fast  $\text{Li}^+$  ion transport and uniform Li electrodeposition. Metals with high melting temperature and low solubility in Li would be preferred to form a stable intermetallic layer on the anode surface.

## Author Contributions

Nicolas Delaporte: Conceptualization; Formal Analysis; Investigation; Methodology; Supervision; Project administration; Validation; Visualization; Writing – original draft; Writing – review & editing. Alexis Perea: Data curation; Formal analysis; Investigation; Validation; Visualization. Steve Collin-Martin: Resources; Methodology; Investigation. Mireille Léonard: Resources; Investigation. Julie Matton: Resources; Investigation. Vincent Gariepy: Resources; Investigation. Hendrix Demers: Resources; Investigation. Daniel Clément: Resources; Investigation. Etienne Rivard: Resources; Investigation. Ashok Vlijh: Conceptualization; Validation.

## Acknowledgements

This work was financially supported by Hydro-Québec. The laboratory experiments were conducted at the Center of

*Excellence in Transportation, Electrification, and Energy Storage (CETEES).*

## Conflict of Interest

The authors declare no conflict of interest.

## Data Availability Statement

Data sharing is not applicable to this article as no new data were created or analyzed in this study.

**Keywords:** all solid-state batteries • dendrite • lithium metal • lithium polymer batteries • lithium protection • PVD • sputtering

- [1] J.-M. Tarascon, M. Armand, *Nature* **2001**, *414*, 359–367.
- [2] C. Sun, J. Liu, Y. Gong, D. P. Wilkinson, J. Zhang, *Nano Energy* **2017**, *33*, 363–386.
- [3] A. Varzi, R. Raccichini, S. Passerini, B. Scrosati, *J. Mater. Chem. A* **2016**, *4*, 17251–17259.
- [4] W. Xu, J. Wang, F. Ding, X. Chen, E. Nasybulin, Y. Zhang, J.-G. Zhang, *Energy Environ. Sci.* **2014**, *7*, 513–537.
- [5] J. Schnell, T. Günther, T. Knoche, C. Vieider, L. Köhler, A. Just, M. Keller, S. Passerini, G. Reinhart, *J. Power Sources* **2018**, *382*, 160–175.
- [6] J. Janek, W. G. Zeier, *Nat. Energy* **2016**, *1*, 1–4.
- [7] M. Rosso, C. Brissot, A. Teyssot, M. Dollé, L. Sannier, J.-M. Tarascon, R. Bouchet, S. Lascaud, *Electrochim. Acta* **2006**, *51*, 5334–5340.
- [8] K. H. Kim, Y. Iriyama, K. Yamamoto, S. Kumazaki, T. Asaka, K. Tanabe, C. A. J. Fisher, T. Hirayama, R. Murugan, Z. Ogumi, *J. Power Sources* **2011**, *196*, 764–767.
- [9] N. Delaporte, A. Guerfi, H. Demers, H. Lorrmann, A. Paoletta, K. Zaghib, *ChemistryOpen* **2019**, *8*, 192–195.
- [10] R. C. Xu, X. H. Xia, S. Z. Zhang, D. Xie, X. L. Wang, J. P. Tu, *Electrochim. Acta* **2018**, *284*, 177–187.
- [11] D. Bosababu, J. Sivaraj, R. Sampathkumar, K. Ramesha, *ACS Appl. Energ. Mater.* **2019**, *2*, 4118–4125.
- [12] R. Xu, X.-Q. Zhang, X.-B. Cheng, H.-J. Peng, C.-Z. Zhao, C. Yan, J.-Q. Huang, *Adv. Funct. Mater.* **2018**, *28*, 1705838.
- [13] C. Jin, O. Sheng, J. Luo, H. Yuan, C. Fang, W. Zhang, H. Huang, Y. Gan, Y. Xia, C. Liang, J. Zhang, X. Tao, *Nano Energy* **2017**, *37*, 177–186.
- [14] N. Delaporte, Y. Wang, K. Zaghib, *Front. Mater.* **2019**, *6*, 267.
- [15] Z. Gao, S. Zhang, Z. Huang, Y. Lu, W. Wang, K. Wang, J. Li, Y. Zhou, L. Huang, S. Sun, *Chin. Chem. Lett.* **2019**, *30*, 525–528.
- [16] Y. Liu, D. Lin, P. Y. Yuen, K. Liu, J. Xie, R. H. Dauskardt, Y. Cui, *Adv. Mater.* **2017**, *29*, 1605531.
- [17] D. J. Lee, H. Lee, J. Song, M.-H. Ryou, Y. M. Lee, H.-T. Kim, J.-K. Park, *Electrochim. Commun.* **2014**, *40*, 45–48.
- [18] Z. Peng, S. Wang, J. Zhou, Y. Jin, Y. Liu, Y. Qin, C. Shen, W. Han, D. Wang, *J. Mater. Chem. A* **2016**, *4*, 2427–2432.
- [19] M. Bai, K. Xie, B. Hong, K. Yuan, Z. Li, Z. Huang, C. Shen, Y. Lai, *Solid State Ionics* **2019**, *333*, 101–104.
- [20] J. Liang, X. Li, Y. Zhao, L. V. Goncharova, G. Wang, K. R. Adair, C. Wang, R. Li, Y. Zhu, Y. Qian, L. Zhang, R. Yang, S. Lu, X. Sun, *Adv. Mater.* **2018**, *30*, 1804684.
- [21] G. Wang, X. Xiong, D. Xie, X. Fu, Z. Lin, C. Yang, K. Zhang, M. Liu, *ACS Appl. Mater. Interfaces* **2019**, *11*, 4962–4968.
- [22] L. Lin, F. Liang, K. Zhang, H. Mao, J. Yang, Y. Qian, *J. Mater. Chem. A* **2018**, *6*, 15859–15867.
- [23] M. Xie, X. Lin, Z. Huang, Y. Li, Y. Zhong, Z. Cheng, L. Yuan, Y. Shen, X. Lu, T. Zhai, Y. Huang, *Adv. Funct. Mater.* **2020**, *30*, 1905949.
- [24] R. Pathak, K. Chen, A. Gurung, K. M. Reza, B. Bahrami, J. Pokharel, A. Baniya, W. He, F. Wu, Y. Zhou, K. Xu, Q. Qiao, *Nat. Commun.* **2020**, *11*, 93.
- [25] K. Thanner, A. Varzi, D. Buchholz, S. J. Sedlmaier, S. Passerini, *ACS Appl. Mater. Interfaces* **2020**, *12*, 32851–32862.
- [26] E. Kazyak, K. N. Wood, N. P. Dasgupta, *Chem. Mater.* **2015**, *27*, 6457–6462.
- [27] A. C. Kozen, C.-F. Lin, A. J. Pearse, M. A. Schroeder, X. Han, L. Hu, S.-B. Lee, G. W. Rubloff, M. Noked, *ACS Nano* **2015**, *9*, 5884–5892.
- [28] L. Chen, K.-S. Chen, X. Chen, G. Ramirez, Z. Huang, N. R. Geise, H.-G. Steinrück, B. L. Fisher, R. Shahbazian-Yassar, M. F. Toney, M. C. Hersam, J. W. Elam, *ACS Appl. Mater. Interfaces* **2018**, *10*, 26972–26981.
- [29] P. K. Alaboina, S. Rodrigues, M. Rottmayer, S.-J. Cho, *ACS Appl. Mater. Interfaces* **2018**, *10*, 32801–32808.
- [30] R. V. Salvatierra, G. A. López-Silva, A. S. Jalilov, J. Yoon, G. Wu, A.-L. Tsai, J. M. Tour, *Adv. Mater.* **2018**, *30*, 1803869.
- [31] M. Bai, K. Xie, K. Yuan, K. Zhang, N. Li, C. Shen, Y. Lai, R. Vajtai, P. Ajayan, B. Wei, *Adv. Mater.* **2018**, *30*, 1801213.
- [32] Y. J. Zhang, X. Y. Liu, W. Q. Bai, H. Tang, S. J. Shi, X. L. Wang, C. D. Gu, J. P. Tu, *J. Power Sources* **2014**, *266*, 43–50.
- [33] T. S. Sudarshan, J. J. Stiglich, *Surface Modification Technologies: Proceedings of the 19th International Conference on Surface Modification Technologies*, August 1–3, 2005, Radisson Riverfront Hotel, St. Paul, Minnesota, USA, ASM International, ASM International, **2006**.
- [34] E. Reinhold, J. Richter, U. Seyfert, C. Steuer, *Surf. Coat. Technol.* **2004**, 188–189, 708–713.
- [35] A. Mukanova, A. Nurpeissova, S.-S. Kim, M. Myronov, Z. Bakenov, *ChemistryOpen* **2018**, *7*, 92–96.
- [36] E. Evshchik, D. Novikov, A. Levchenko, S. Nefedkin, A. V. Shikhovtseva, O. V. Bushkova, Y. A. Dobrovolsky, *Int. J. Electrochem. Sci.* **2018**, *13*, 2860–2874.
- [37] S. Ulusoy, S. Gulen, G. Aygun, L. Ozdemir, *Solid State Ionics* **2018**, *324*, 226–232.
- [38] J. Sastre, A. Priebe, M. Döbeli, J. Michler, A. N. Tiwari, Y. E. Romanyuk, *Adv. Mater. Interfaces* **2020**, *7*, 2000425.
- [39] A. Heckmann, M. Krott, B. Streipert, S. Uhlenbruck, M. Winter, T. Placke, *ChemPhysChem* **2017**, *18*, 156–163.
- [40] S. Wang, K. V. Kravchyk, A. N. Filippin, R. Widmer, A. N. Tiwari, S. Buecheler, M. I. Bodnarchuk, M. V. Kovalenko, *ACS Appl. Energ. Mater.* **2019**, *2*, 974–978.
- [41] P. Coddet, M.-L. Amany, J. Vulliet, A. Caillard, A.-L. Thomann, *Surf. Coat. Technol.* **2019**, *357*, 103–113.
- [42] T. Zerrin, M. Kurban, M. M. Dickson, M. Ozkan, C. S. Ozkan, *ACS Appl. Energ. Mater.* **2020**, *3*, 1515–1529.
- [43] I.-K. Ahn, Y.-J. Lee, S. Na, S.-Y. Lee, D.-H. Nam, J.-H. Lee, Y.-C. Joo, *ACS Appl. Mater. Interfaces* **2018**, *10*, 2242–2248.
- [44] L. Li, S. Liu, H. Zhou, Q. Lei, K. Qian, *Mater. Lett.* **2018**, *216*, 135–138.
- [45] H.-S. Kim, Y. Oh, K. H. Kang, J. H. Kim, J. Kim, C. S. Yoon, *ACS Appl. Mater. Interfaces* **2017**, *9*, 16063–16070.
- [46] C. M. Julien, A. Mauger, O. M. Hussain, *Mater.* **2019**, *12*, 2687.
- [47] M. Hallot, A. Demortière, P. Roussel, C. Lethien, *Energy Storage Mater.* **2018**, *15*, 396–406.
- [48] J. Trask, A. Anapolksky, B. Cardozo, E. Januar, K. Kumar, M. Miller, R. Brown, R. Bhardwaj, *J. Power Sources* **2017**, *350*, 56–64.
- [49] L. Wang, Q. Wang, W. Jia, S. Chen, P. Gao, J. Li, *J. Power Sources* **2017**, *342*, 175–182.
- [50] L. Wang, L. Zhang, Q. Wang, W. Li, B. Wu, W. Jia, Y. Wang, J. Li, H. Li, *Energy Storage Mater.* **2018**, *10*, 16–23.
- [51] R. A. Huggins, *J. Power Sources* **2018**, *22*, 341–350.
- [52] X. Liao, Q. Liu, X. Liu, S. Zhu, K. Zhao, Y. Zhao, *Phys. Chem. Chem. Phys.* **2022**, *24*, 4751–4758.
- [53] S. Qu, W. Jia, Y. Wang, C. Li, Z. Yao, K. Li, Y. Liu, W. Zou, F. Zhou, Z. Wang, J. Li, *Electrochim. Acta* **2019**, *317*, 120–127.
- [54] W. Tang, X. Yin, S. Kang, Z. Chen, B. Tian, S. L. Teo, X. Wang, X. Chi, K. P. Loh, H.-W. Lee, G. W. Zheng, *Adv. Mater.* **2018**, *30*, 1801745.
- [55] Q. Tang, H. Li, Y. Pan, J. Zhang, Y. Chen, *Ionics* **2019**, *25*, 2525–2533.
- [56] M. C. Stan, J. Becking, A. Kolesnikov, B. Wankmiller, J. E. Frerichs, M. R. Hansen, P. Bieker, M. Kolek, M. Winter, *Mater. Today* **2020**, *39*, 137–145.
- [57] J. Deng, Y. Wang, S. Qu, Y. Liu, W. Zou, F. Zhou, A. Zhou, J. Li, *Batteries & Supercaps* **2021**, *4*, 140–145.
- [58] P. Hovington, V. Timoshevskii, S. Burgess, H. Demers, P. Statham, R. Gauvin, K. Zaghib, *Scanning* **2016**, *38*, 571–578.
- [59] N. Delaporte, G. Lajoie, A. Darwiche, M.-J. Vigeant, S. Collin-Martin, D. Clément, *RSC Adv.* **2022**, *12*, 15493–15507.
- [60] Distinguishing charge rates for next-generation batteries, Blog Post. (2021). <https://www.quantumescape.com/resources/blog/distinguishing-charge-rates-for-next-generation-batteries/>.
- [61] G. Bridgewater, M. J. Capener, J. Brandon, M. J. Lain, M. Copley, E. Kendrick, *Batteries* **2021**, *7*, 38.

- [62] P. Gu, X. Zhu, J. Li, H. Wu, D. Yang, *J. Mater. Sci. Mater. Electron.* **2018**, *29*, 9893–9900.
- [63] M. Khojasteh, V. V. Kresin, *Appl. Nanosci.* **2017**, *7*, 875–883.
- [64] A. M. Engwall, L. B. Bayu Aji, A. A. Baker, S. J. Shin, J. H. Bae, S. K. McCall, J. D. Moody, S. O. Kucheyev, *Appl. Surf. Sci.* **2021**, *547*, 149010.
- [65] N. Aghilizadeh, A. H. Sari, D. Dorranian, *J. Theor. Appl. Phys.* **2017**, *11*, 285–290.
- [66] A. Paul, J. Wingbermuhle, *Appl. Surf. Sci.* **2006**, *252*, 8151–8155.
- [67] N. Delaporte, G. Lajoie, S. Collin-Martin, K. Zaghib, *Sci. Rep.* **2020**, *10*, 3812.
- [68] H. Joachin, T. D. Kaun, K. Zaghib, J. Prakash, *J. Electrochem. Soc.* **2009**, *156*, A401–406.
- [69] G. Homann, L. Stoltz, K. Neuhaus, M. Winter, J. Kasnatscheew, *Adv. Funct. Mater.* **2020**, *30*, 2006289.
- [70] G. Homann, L. Stoltz, J. Nair, I. C. Laskovic, M. Winter, J. Kasnatscheew, *Sci. Rep.* **2020**, *10*, 4390.
- [71] N. Delaporte, A. Pereira, E. Lebègue, S. Ladouceur, K. Zaghib, D. Bélanger, *ACS Appl. Mater. Interfaces* **2015**, *7*, 18519–18529.
- [72] R. Suárez-Hernández, G. Ramos-Sánchez, I. O. Santos-Mendoza, G. Guzmán-González, I. González, *J. Electrochem. Soc.* **2020**, *167*, 100529.
- [73] N. Suzuki, N. Yashiro, S. Fujiki, R. Omoda, T. Shiratsuchi, T. Watanabe, Y. Aihara, *Adv. Energy Sustain. Res.* **2021**, *2*, 2100066.
- [74] Y.-G. Lee, S. Fujiki, C. Jung, N. Suzuki, N. Yashiro, R. Omoda, D.-S. Ko, T. Shiratsuchi, T. Sugimoto, S. Ryu, J. H. Ku, T. Watanabe, Y. Park, Y. Aihara, D. Im, I. T. Han, *Nat. Energy* **2020**, *5*, 299–308.
- [75] Y. Zhang, S. Wang, E. Lordan, K. Dou, X. Zhou, T. Hashimoto, *J. Alloys Compd.* **2022**, *895*, 162219.
- [76] H. Zhao, F. De Geuser, A. Kwiatkowski da Silva, A. Szczepaniak, B. Gault, D. Ponge, D. Raabe, *Acta Mater.* **2018**, *156*, 318–329.
- [77] K. Edalati, Z. Horita, R. Z. Valiev, *Sci. Rep.* **2018**, *8*, 6740.
- [78] T. Mitsuhashi, Y. Ito, Y. Takeuchi, S. Harada, T. Ujihara, *Thin Solid Films* **2015**, *590*, 207–213.
- [79] K. Ishikawa, Y. Ito, S. Harada, M. Tagawa, T. Ujihara, *Cryst. Growth Des.* **2017**, *17*, 2379–2385.
- [80] K. Ishikawa, S. Harada, M. Tagawa, T. Ujihara, *ACS Appl. Mater. Interfaces* **2020**, *12*, 9341–9346.
- [81] H. Toku, R. S. Pessoa, T. B. Liberato, M. Massi, H. S. Maciel, A. S. da Silva Sobrinho, *ECS Trans.* **2007**, *9*, 189–197.
- [82] Y. Ouyang, C. Cui, Y. Guo, Y. Wei, T. Zhai, H. Li, *ACS Appl. Mater. Interfaces* **2020**, *12*, 25818–25825.

Manuscript received: June 1, 2022

Revised manuscript received: June 22, 2022

Accepted manuscript online: June 23, 2022

Version of record online: July 8, 2022